Electronic Supplementary Material

Construction of nitrogen-doped carbon cladding $LiMn_2O_4$ film electrode with enhanced stability for electrochemically selective extraction of lithium ions

Jiahui Ren[1], Yongping He[2], Haidong Sun[2], Rongzi Zhang[2], Juan Li[2], Wenbiao Ma[1], Zhong Liu[3], Jun Li[3], Xiao Du (✉)[1], Xiaogang Hao (✉)[1]

1 College of Chemical Engineering and Technology, Taiyuan University of Technology, Taiyuan 030024, China

2 Academia Sinica, Qinghai Salt Lake Industry Group Company Limited, Geermu 816000, China

3 Qinghai Institute of Salt Lakes Chinese Academy of Sciences, Xining 810008, China

E-mails: xghao@tyut.edu.cn (Hao X); duxiao@tyut.edu.cn (Du X)

Contents:

Characterizations

The micro-morphologies of materials were observed by field-emission scanning electron microscopy (SEM, JSM-6510, Japan) and high-resolution transmission electron microscope (HRTEM, Tecnai G2 F20, USA). The crystalline structure was determined by a powder X-ray diffraction instrument (XRD, MiniFlex600, Japan) which used a Cu Ka radiation source over a 2θ range of 5° to 90°. Fourier transform infrared spectroscopy (FT-IR) was recorded by Nicolet iS20 using a KBr pellet in the range of 400-4000 cm^{-1}. Raman spectroscopy (Horiba Scientific LabRAM HR Evolution, France) was analyzed with the argon-ion laser of 532 nm wavelength. X-ray photoelectron spectroscopy (XPS, Thermo Scientific K-Alpha, USA) was used to obtain the Mn valence information. N_2 adsorption-desorption isotherm and pore size distribution were measured at 77 K by an N_2 adsorption system (JW-BK122W, JWGB Sci.& Tech. Co.Ltd, Beijing). The weight change of the C-N@LMO by heating it to 700℃ was determined by using a thermogravimetric analyzer (TGA, Netzsch STA 449 F5, Germany) at a ramping rate of 10℃ min^{-1} under air atmosphere. The electrochemical performance was measured in a VMP3 Potentiostat (Princeton, USA) instrument controlled by EC-Lab software. Electrical resistivity was determined by a Four-probe resistivity tester (SZT-2A, Suzhou Tongchuang Electronics Co., Ltd., China).

Density functional theory (DFT) calculation

The Dmol3 software package was used to perform all density functional theory (DFT) calculations [1]. Electron-ion interactions were described by using all-electron potentials. The electron interactions were described using the Perdew-Burke-Ernzerhof (PBE) exchange-correlation functional of the generalized gradient approximation (GGA) [2, 3], and the wave functions were expanded using the double numerical polarized (DNP) basis set. In the optimization process, all atoms are allowed to relax freely with a global orbital cutoff of 5.2 Å. The convergence threshold for the electronic self-consistent field (SCF) loop and residual forces in this study was set at 1.0×10^{-5} eV/atom and 0.002 Ha/Å, respectively.

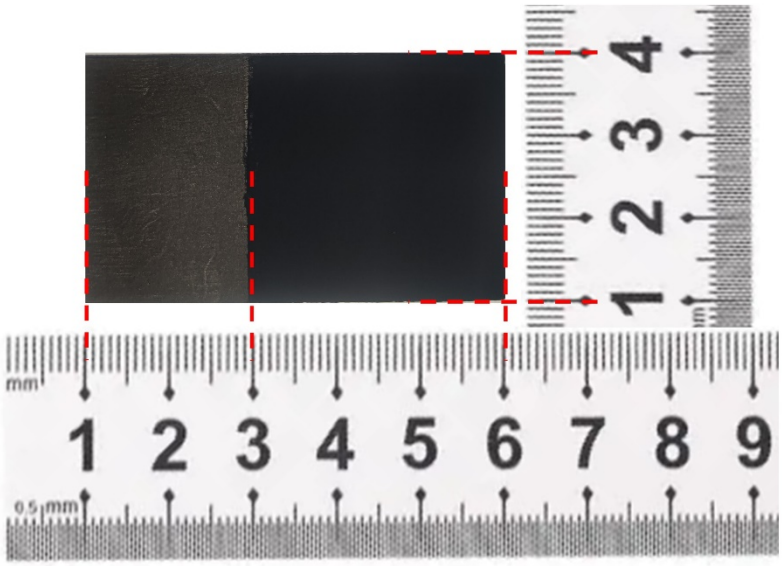

Fig. S1. The practical image of the film electrode.

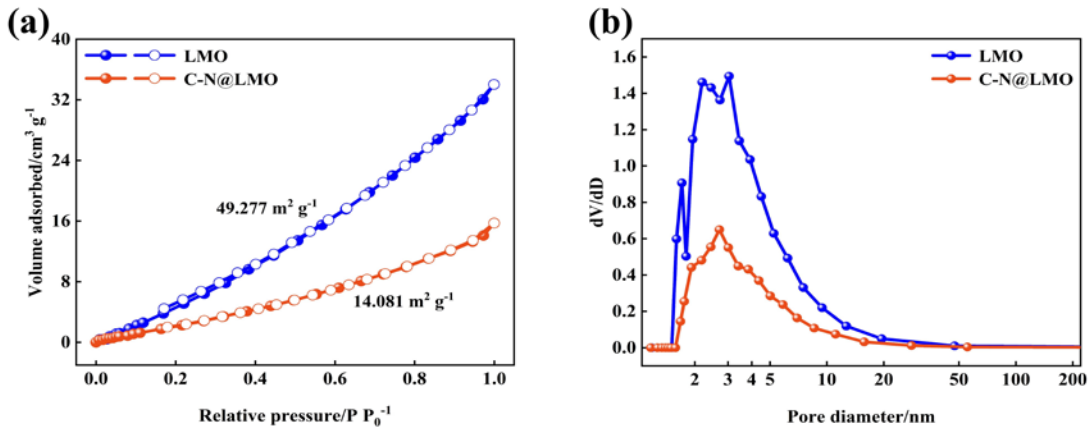

Fig. S2. N_2 adsorption-desorption isotherm (a) and pore size distribution (b) of LMO and C-N@LMO.

N_2 adsorption-desorption isotherm and the pore size distribution analysis of the LMO and C-N@LMO are investigated. As shown in Fig. S2a, the curves for the LMO and C-N@LMO displayed the not typical II-type isotherm, which were agreed with the nonporous material [4]. This is because the carbon cladding layer formed by the pyrolysis of PPy is continuous and has no visible holes, which is why it can be protected. However, the specific surface area of the material decreases after cladding, because for nonporous materials, the larger the particle size (as shown in SEM, the presence of the cladding layer makes the particle size of the material larger), the smaller the specific surface area [5]. The pore size distributions are reported by Barrett-Joyner-Halenda (BJH) tests [6], which showed that the pores may be formed due to particle buildup rather than actual presence on the material surface. The number of pores in C-N@LMO is reduced compared to LMO, which indicates that the encapsulated C-

N layer makes the particles more closely connected to each other, resulting in faster ions and electronics conduction rates.

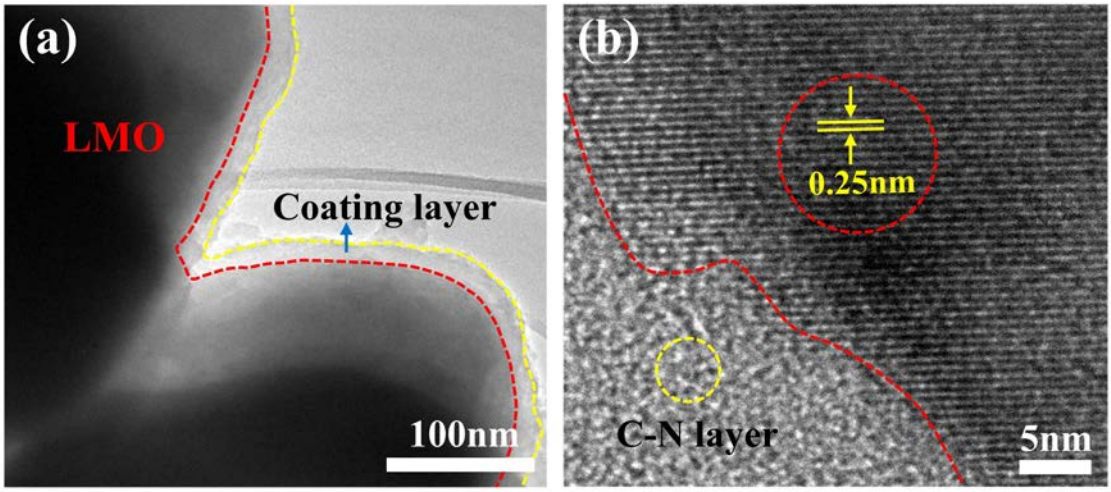

Fig. S3. (a) TEM image and (b) HRTEM image of C-N@LMO.

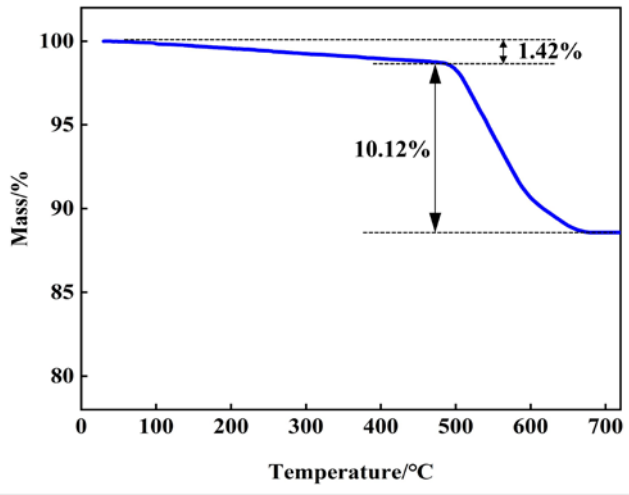

Fig. S4. TGA curve of C-N@LMO between 30 and 720°C with a heating rate of 10°C min^{-1} in air atmosphere.

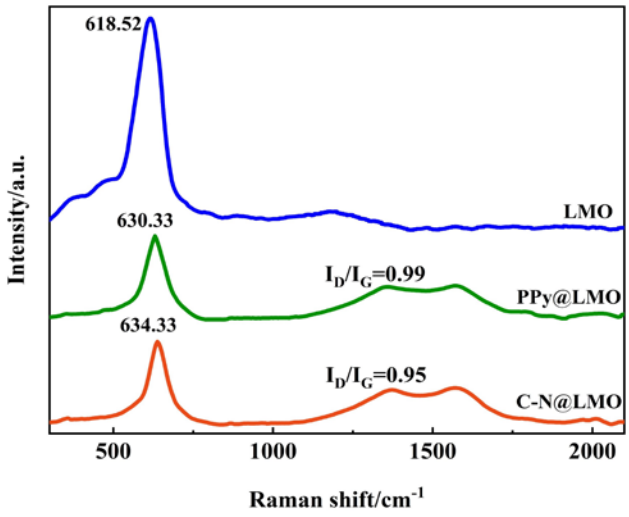

Fig. S5. Raman spectra of LMO, PPy@LMO, and C-N@LMO.

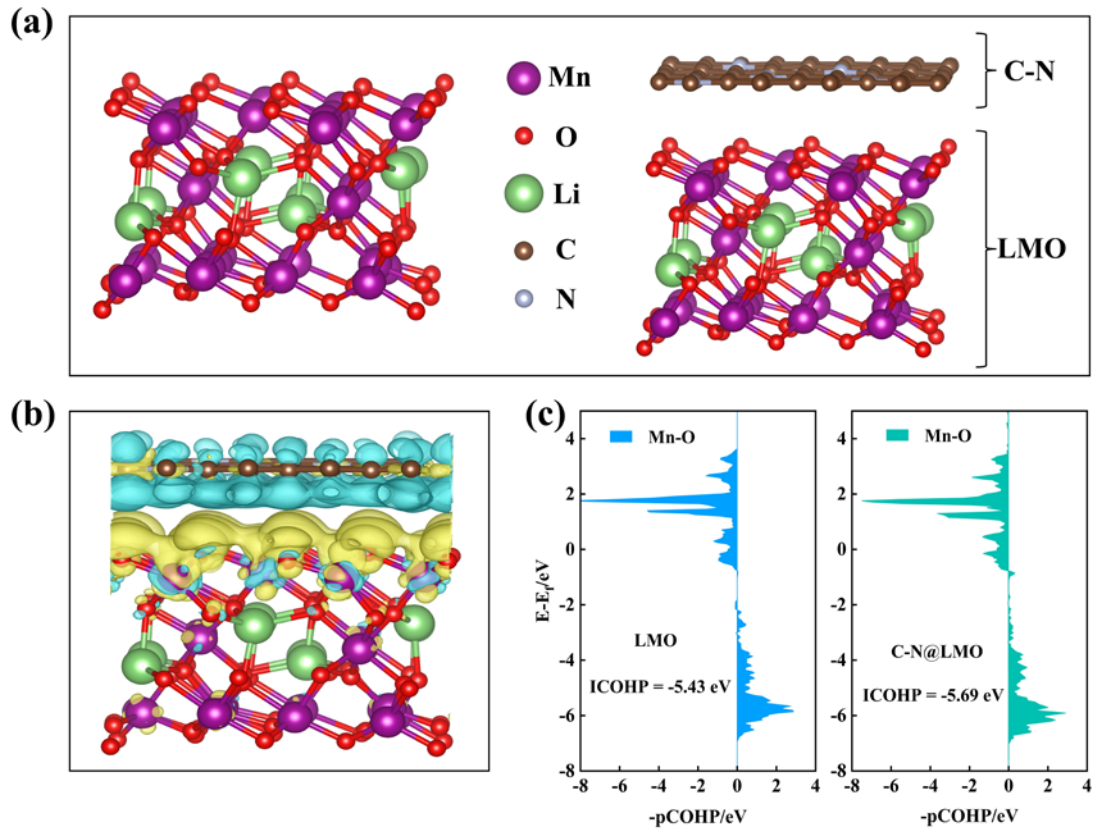

Fig. S6. (a) The structural models of LMO and C-N@ LMO; (b) charge density difference of C-N@ LMO (yellow represents the electron-aggregating region, blue represents the electron-deficient region); (c) COHP diagrams of LMO and C-N@ LMO.

As shown in Fig. S6a, we constructed the structural models of LMO and C-N coated LMO (C-N@ LMO), respectively. The charge density difference (Fig. S6b) clearly shows that the surface cladding

caused the directional movement of electrons in the system and electrons migrated from the C-N layer to LMO. Further, we calculated the projected crystal orbital Hamiltonian populations (COHP) of the Mn-O bonds before and after the C-N layer cladding (Fig. S6c), and the ICOHP values can reflect the bond strength visually. The calculations show that more electrons filled the bonding orbital of Mn-O bonds after C-N layer cladding, and the ICOHP value of C-N@ LMO (-5.69 eV) was more negative than that of LMO (-5.43 eV), which indicates the stronger Mn-O bonding strength in C-N@ LMO. In summary, the coverage of the C-N layer leads to the transfer of electrons and fills the bonding orbitals of the Mn-O bond, which in turn leads to a more stable bonding.

Table S1. The content and ratio of Mn^{3+} and Mn^{4+} in different film electrodes [7].

	Mn^{3+}		Mn^{4+}		Mn^{4+}/Mn^{3+}
	$2p_{1/2}$	$2p_{3/2}$	$2p_{1/2}$	$2p_{3/2}$	
(1)	0.25	0.52	0.32	0.48	1.039
(2)	0.23	0.47	0.36	0.42	1.114
(3)	0.25	0.51	0.33	0.49	1.079

Table S2. Comparison of ionic radius and the diffusion energy barriers of Li^+ and Mg^{2+} [8, 9].

Ion type	Ionic radius (nm)	Diffusion energy barrier (eV)
Li^+	0.076	1.09
Mg^{2+}	0.072	1.53

Table S3. A brief comparison of electrochemical methods for Lithium recovery based on Li^+ ion exchangers.

Li^+ exchangers	Intercalation Capacity (mg g^{-1})	Li^+/Mg^{2+} Separation factors	Ref.
C-N@LMOE	21.7	118.38	This work
$Li_{1-x}Mn_2O_4$	22.0	74.03	[10]
$Li_{1-x}Ni_{1/3}Co_{1/3}Mn_{1/3}O_2$	10.8	42.87	[11]
LIIP@N-CMS/GA	41.1	14.37	[12]
$H_{1.6}Mn_{1.6}O_4$/rGO	9.6	10.23	[13]
λ-MnO_2	7.3	5.57	[14]

Table S3 shows the characteristic parameters of different electrochemical methods for the selective recovery of Li^+ ions based on various electrode materials. Although the experimental results under different conditions cannot be directly compared, the calculated separation factors for Li^+/Mg^{2+} of this work were indeed at a high level compared with those of reported Li^+ ion exchangers. Nevertheless, the overall results demonstrated that the λ-MnO_2/rGO/Ca-alg composite electroactive film could be expected to be applied for the recovery of lithium ions from brine in a practical process.

References

1. B. Delley. From molecules to solids with the DMol3 approach. The Journal of Chemical Physics, 2000, 113, 7756-7764

2. Matveev A, Staufer M, Mayer M. Density functional study of small molecules and transition-metal carbonyls using revised PBE functionals. International Journal of Quantum Chemistry, 2015, 75(4): 863-873

3. Perdew J, Chevary J, Vosko S, Jackson K, Pederson M, Singh D, Fiolhais C. Erratum: Atoms, molecules, solids, and surfaces: Applications of the generalized gradient approximation for exchange and correlation. Physical Review B Condensed Matter, 1993, 46(11): 6671-6687

4. Ma W, Du X, Liu M, Gao F, Ma X, Li Y, Guan G, Hao X. A conductive chlorine ion-imprinted polymer threaded in metal-organic frameworks for electrochemically selective separation of chloride ions. Chemical Engineering Journal, 2021, 412: 128576

5. Li S, Zhang J, Yan Y, Yu L, Zhao J. Manganese valence state regulated beta-manganese dioxide porous nanoflowers as high-performance cathodes at large current densities for aqueous magnesium ions battery capacitor. Journal of Energy Storage, 2023, 59: 106456

6. Zhang Z, Du X, Wang Q, Gao F, Jin T, Hao X, Ma P, Li J, Guan G. A scalable three-dimensional porous λ-MnO_2/rGO/Ca-alginate composite electroactive film with potential-responsive ion-pumping effect for selective recovery of lithium ions. Separation and Purification Technology, 2021, 259: 118111

7. Jiang Y, Chai L, Zhang D, Ouyang F, Zhou X, Alhassan S, Liu S, He Y, Yan L, Wang H, Zhang W. Facet-Controlled $LiMn_2O_4$/C as deionization electrode with enhanced stability and high desalination performance. Nano-Micro Letters, 2022, 14, 176

8. Zhang H, Du X, Ding S, Wang Q, Chang L, Ma X, Hao X, Pen C. DFT calculations of the synergistic effect of λ-MnO_2/graphene composites for electrochemical adsorption of lithium ions. Physical Chemistry Chemical Physics, 2019, 21(15): 8133-8140

9. Zhao A, Liu J, Ai X, Yang H, Cao Y. Highly selective and pollution-free electrochemical extraction of lithium by a polyaniline/$Li_xMn_2O_4$ cell. ChemSusChem, 2019, 12(7): 1361-1367

10. Zhao M, Ji Z, Zhang Y, Guo Z, Zhao Y, Liu J, Yuan J. Study on lithium extraction from brines based on $LiMn_2O_4$/$Li_{1-x}Mn_2O_4$ by electrochemical method. Electrochimical Acta, 2017, 252: 350-361

11. Lawagon C, Nisola G, Cuevas R, Kim H, Lee S, Chung W. $Li_{1-x}Ni_{0.33}Co_{1/3}Mn_{1/3}O_2$/Ag for electrochemical lithium recovery from brine. Chemical Engineering Journal, 2018, 348: 1000-1011

12. Zhang E, Liu W, Liang Q, Liu X, Zhao Z, Yang Y. Selective recovery of Li^+ in acidic environment based on one novel electroactive Li^+-imprinted graphene-based hybrid aerogel. Chemical Engineering

Journal, 2020, 385: 123948

13. Wang Q, Du X, Gao F, Liu F, Liu M, Hao X, Tang K, Guan G, Abudula A. A novel $H_{1.6}Mn_{1.6}O_4$/reduced graphene oxide composite film for selective electrochemical capturing lithium ions with low concentration. Separation and Purification Technology, 2019, 226: 59-67

14. Kim S, Joo H, Moon T, Kim S, Yoon J. Rapid and selective lithium recovery from desalination brine using an electrochemical system. Environmental Science: Processes & Impacts, 2019, 21: 667-676